JGR Solid Earth

RESEARCH ARTICLE
10.1029/2025JB031225

Strong Fault Interaction in Double-Vergence Structure: Lessons From the 2022 Yuli Earthquake and the 2022 Chihshang Earthquake, Eastern Taiwan

Yuri Ishimaru[1], **Youichiro Takada**[2], **Kuo-En Ching**[3], **and Wu-Lung Chang**[4]

[1]Department of Natural History Sciences, Hokkaido University, Sapporo, Japan, [2]Department of Earth and Planetary Sciences, Hokkaido University, Sapporo, Japan, [3]Department of Geomatics, National Cheng Kung University, Tainan, Taiwan, [4]Department of Earth Sciences, National Central University, Taoyuan, Taiwan

Key Points:

- Almost pure dip-slip of the Yuli earthquake on the east-dipping Longitudinal Valley Fault in eastern Taiwan is estimated by InSAR and GNSS
- The Yuli earthquake increased Coulomb stress in main rupture area of the Chihshang earthquake on the west-dipping Central Range Fault
- Dip-slip earthquakes on one fault promote earthquakes on the other fault while strike-slips suppress those in double-vergence fault system

Supporting Information:

Supporting Information may be found in the online version of this article.

Correspondence to:

Y. Ishimaru,
ishimaru.yuri.c4@elms.hokudai.ac.jp

Citation:

Ishimaru, Y., Takada, Y., Ching, K.-E., & Chang, W.-L. (2025). Strong fault interaction in double-vergence structure: Lessons from the 2022 Yuli earthquake and the 2022 Chihshang earthquake, eastern Taiwan. *Journal of Geophysical Research: Solid Earth*, *130*, e2025JB031225. https://doi.org/10.1029/2025JB031225

Received 21 JAN 2025
Accepted 3 JUL 2025

Author Contributions:

Conceptualization: Youichiro Takada, Kuo-En Ching
Data curation: Yuri Ishimaru, Wu-Lung Chang
Formal analysis: Yuri Ishimaru, Wu-Lung Chang
Funding acquisition: Youichiro Takada
Investigation: Yuri Ishimaru, Youichiro Takada
Methodology: Yuri Ishimaru, Youichiro Takada, Wu-Lung Chang
Project administration: Youichiro Takada
Resources: Kuo-En Ching, Wu-Lung Chang

Abstract The Longitudinal Valley Fault (LVF) and the Central Range Fault (CRF) in eastern Taiwan consist of a head-to-head double-vergence structure hosting disastrous earthquakes. It was previously proposed that the fault slip on one of these faults suppresses the earthquake generation on the other. Nonetheless, the 2022 Chihshang earthquake (M_w 7.0) on the CRF occurred soon after the 2022 Yuli earthquake (M_w 6.7) on the LVF. Here, we provide a comprehensive framework of the fault interaction consistently explaining these contradictory findings. First, we estimated the coseismic slip distribution of the Yuli earthquake from Global Navigation Satellite System (GNSS) and L-band satellite interferograms. The results indicate almost pure reverse faulting. Second, with the estimated slip distribution, we calculated changes in Coulomb failure function (ΔCFF) on the CRF due to the Yuli earthquake on the LVF. The ΔCFF reaches +0.25 MPa around the main rupture area of the Chihshang earthquake, which is equivalent to the clock advance of 36–100 years, suggesting a large impact on the earthquake generation cycles. Finally, we found that a rake angle of fault slip has a significant effect on the ΔCFF on the other fault in the double-vergence structure: it takes large positive values when 90° like the Yuli earthquake, but almost negative when 45° or less, which comprehensively explains the seismic quiescence previously reported and the positive ΔCFF on the CRF caused by the Yuli earthquake. The strong impact of the rake angle is also supported by the temporal distribution of historical earthquakes in eastern Taiwan.

Plain Language Summary The Longitudinal Valley Fault (LVF) and the Central Range Fault (CRF) in eastern Taiwan are hosts of disastrous earthquakes. These are closely located and dip in opposite directions (inverted V-shaped). It was previously proposed that earthquakes on one of these faults suppress earthquakes on the other. Nonetheless, the 2022 Chihshang earthquake (M_w 7.0) on the CRF occurred soon after the 2022 Yuli earthquake (M_w 6.7) on the LVF. We comprehensively understand these contradictory findings by focusing on the fault slip directions. First, we revealed almost pure reverse faulting of the LVF during the Yuli earthquake from geodetic observations. According to our simulation, the Yuli earthquake imparted the stress equivalent to a steady stress accumulation of 36–100 years around the main rupture area of the Chihshang earthquake on the CRF, suggesting a large impact on the earthquake generation. Finally, we demonstrated the importance of slip directions on the fault interaction within the inverted V-shaped fault systems: reverse slip prompts earthquakes on the other fault while lateral slip suppresses. The effect of the slip direction consistently explains both the previously suggested seismic quiescence and the promotion of the Chihshang earthquake by the Yuli earthquake. This mechanism is also consistent with historical seismicity.

1. Introduction

Earthquake recurrence is ideally explained by the classical elastic theory (Reid, 1910), that is, the repetition of shear stress release and accumulation. For example, the Alpine Fault in New Zealand, which is characterized by isolated structures, tends to exhibit almost periodic earthquake generation (Berryman et al., 2012). The recurrence interval of earthquakes, however, is often affected by the activities of nearby faults because those activities alter the surrounding stress field (Freed, 2005; Harris, 1998; Stein, 1999; Tang et al., 2023; Toda & Stein, 2020). Understanding the nearby fault interaction is therefore key to evaluating seismic hazards. To untangle the complex nature of the fault interaction, it is favorable to focus on the fault systems with active seismicity. Here we focus on the eastern part of Taiwan which is characterized by two closely located faults with active seismicity.

Software: Yuri Ishimaru, Wu-Lung Chang
Supervision: Youichiro Takada
Validation: Youichiro Takada, Kuo-En Ching, Wu-Lung Chang
Visualization: Yuri Ishimaru
Writing – original draft: Yuri Ishimaru
Writing – review & editing: Youichiro Takada, Kuo-En Ching, Wu-Lung Chang

Taiwan is one of the fastest-growing orogens on Earth which is essentially driven by the collision between the Luzon Arc on the Philippine Sea Plate and the Chinese continental margin on the Eurasian Plate (e.g., Chai, 1972; Rau & Wu, 1995; Takada et al., 2007) (Figure 1). The convergent boundary is located in eastern Taiwan which is characterized by the north-south running Longitudinal Valley bounding volcanic rocks in the Coastal Range and highly metamorphosed rocks in the Central Range (Ho, 1986). A pair of oppositely dipping faults run in this collision boundary: the east-dipping Longitudinal Valley Fault (LVF) (Angelier et al., 1997; Shyu, Sieh, Avouac, et al., 2006; Thomas et al., 2014) and the west-dipping Central Range Fault (CRF) (Lee et al., 2023; Shyu, Sieh, Chen, & Chung, 2006). These faults are located nearby and the surface traces are almost parallel (Figure 1). Their cross-section takes an inversed V-shape geometry, often described as "head-to-head double-vergence" or simply "double-vergence" fault structure (He et al., 2024; Tang et al., 2023; Tung et al., 2025; Yang et al., 2024). In this paper, we use "double-vergence structure."

The LVF and the CRF have strongly interacted with each other due to their proximity. The interaction between these faults is reported such that an earthquake on one fault induces seismic quiescence on the other (Tang et al., 2023), which is statistically supported by a numerical simulation (Hsu & Wu, 2025). However, three major earthquakes successively occurred on both faults in 2022 (Figure 1; Table 1), which is a counter-example of the reported fault interaction. The Yuli earthquake (M_w 6.7) on 22 March 2022 (UTC) occurred on the LVF (Peng et al., 2023), while the Guanshan earthquake (M_w 6.5) on 17 September 2022 and the Chihshang earthquake (M_w 7.0) on 18 September 2022 occurred on the CRF (He et al., 2024; Lee et al., 2023; Tang et al., 2023; Tung et al., 2025; Yagi et al., 2023; Yang et al., 2024). Therefore, a more comprehensive framework is needed to understand the kinematic interaction between the LVF and the CRF.

In this study, we attempt to add new perspectives on kinematic fault interaction between the LVF and the CRF by focusing on the 2022 Yuli earthquake and the 2022 Chihshang earthquake. To reveal the slip distribution of the Yuli earthquake, we first constructed a coseismic source model from a combination of Global Navigation Satellite System (GNSS) and Interferometric Synthetic Aperture Radar (InSAR). The procedure for processing GNSS and InSAR data is described in Chapter 2. In Chapter 3, we explained the mathematical procedure to estimate the fault slip of the Yuli earthquake from the dense geodetic data set. Based on the estimated slip distribution, we quantitatively estimate the effect of the Yuli earthquake on the Chihshang earthquake that occurred on the CRF in Chapter 4. From a general viewpoint, in Chapter 5, we propose a physical mechanism in a double-vergence fault system, which provides a comprehensive understanding of the contradictory findings by focusing on the slip directions.

2. Materials and Methods

2.1. GNSS Data

To obtain the coseismic displacements of the Yuli earthquake, we used 44 continuous Global Navigation Satellite Systems (GNSS) stations located in 23–23.9°N and 120.8–121.7°E (Figure S1 in Supporting Information S1). These stations are maintained by Central Geological Survey (CGS), Central Weather Administration (CWA), National Land Surveying and Mapping Center (NLSC), and Academia Sinica (IESAS). First, we calculated the daily coordinates of the stations within the framework of International Terrestrial Reference Frame (ITRF2014) (Altamimi et al., 2016) by Precise Point Positioning (PPP) (Zumberge et al., 1997) using GipsyX software (Bertiger et al., 2020). Next, we estimated the coseismic displacements by averaging the coordinates of 5 days before and after the Yuli earthquake (22 March 2022, UTC), respectively, and subtracted the former from the latter. The displacements at all stations are referenced to S01R (23.66°N, 119.59°E) in Penghu Island off the western coast of Taiwan (Figure S1 in Supporting Information S1), located on the Chinese stable continental margin. The coseismic displacements and associated standard deviations are listed in Table S1 of Supporting Information S1. We excluded four stations (CHUL, DSIN, DULI, and FENP) with horizontal standard deviations greater than 2 cm or a vertical standard deviation greater than 4 cm. We used the rest of the 40 stations for the fault slip inversion in Chapter 3. The coseismic displacements observed at the 40 GNSS stations (Figure 2) indicate eastward movement toward the hypocentral area and the surface uplift of the Coastal Range relative to the Longitudinal Valley.

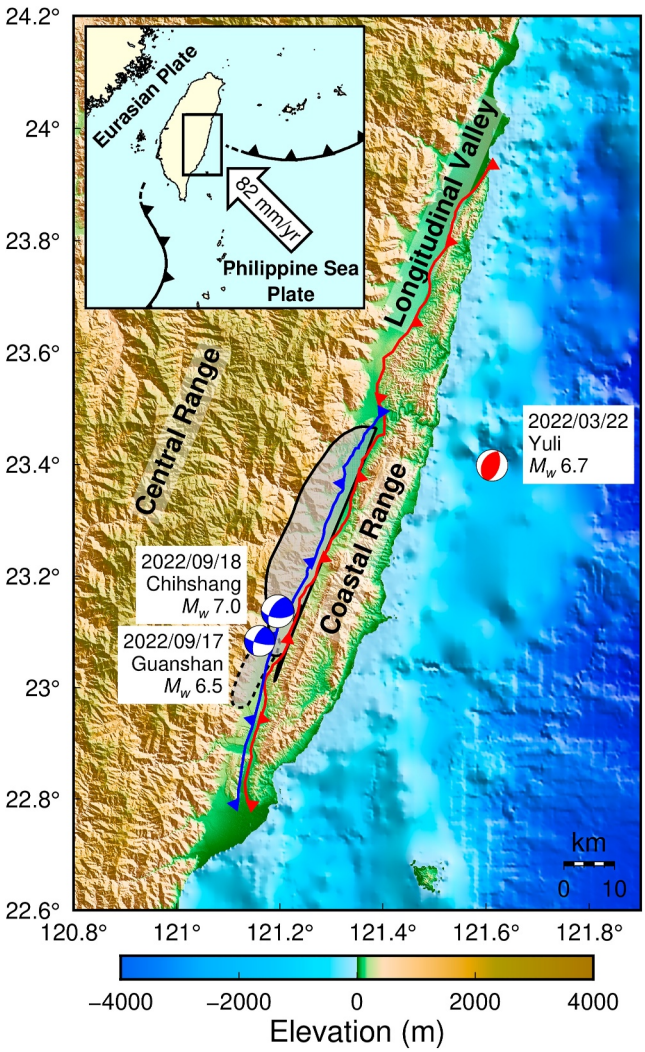

Figure 1. Tectonic settings of eastern Taiwan. Red and blue lines indicate the surface trace of the LVF and the CRF, respectively (Styron & Pagani, 2020). A red beachball indicates the focal mechanism of the Yuli earthquake that occurred on the LVF. Blue beachballs indicate those of the Guanshan earthquake and the Chihshang earthquake that occurred on the CRF. The dashed and the solid contours indicate a slip amount of 50 cm associated with the Guanshan earthquake and the Chihshang earthquake, respectively (Tang et al., 2023). The elevation is provided by Shuttle Radar Topography Mission (SRTM 1S and SRTM15 + V2) (Tozer et al., 2019).

2.2. InSAR Images

The GNSS stations are very sparse in the Central Range (Figure S1 in Supporting Information S1) because steep topography is disadvantageous for ground-based geodetic surveys. Hence, we make the most of the Interferometric Synthetic Aperture Radar (InSAR) analysis which does not require any ground-based surveys. We used ScanSAR data obtained by Advanced Land Observing Satellite 2 (ALOS-2), which was launched by Japan Aerospace Exploration Agency (JAXA). ALOS-2 steadily provides high quality data even in mountainous areas due to long-wavelength radio waves (L-band) penetrating dense vegetation.

We made four independent interferograms (Table 2) using the GAMMA Software (Wegmüller & Werner, 1997) and the 30 m grid ASTER Global Digital Elevation Model (GDEM) Version 3 (Abrams et al., 2020). The look numbers were determined to obtain a ground resolution of approximately 300 m. To exclude the postseismic displacement as much as possible, we selected the interferometric pair of the shortest temporal baseline. The GNSS time series (Figure S2 in Supporting Information S1) indicates that the postseismic displacements are negligible compared to the coseismic displacements (less than 2 cm even at the station closest to the epicenter with the largest displacement).

Even after subtracting the orbital and topographic fringes from the interferograms, strong ionospheric and tropospheric disturbances remain (Figure S3 in Supporting Information S1). L-band interferograms are sensitive to ionospheric disturbances because of the dispersive nature of ionosphere (e.g., Meyer et al., 2006; Wegmüller et al., 2006). In addition, large topographic variations as seen in eastern Taiwan lead to significant tropospheric disturbances on the interferograms (e.g., Tarayre & Massonnet, 1996). To reduce the effects of these disturbances as much as possible, we applied two methods for the ionospheric correction and two methods for the tropospheric correction (i.e., four combinations) to the four interferograms and compared the results. To correct the ionospheric disturbances, we applied third-order polynomial approximation (e.g., Fukushima et al., 2018) and the split spectrum method (SSM) (Brcic et al., 2010; Furuya et al., 2017; Gomba et al., 2016; Rosen et al., 2010; Wegmüller et al., 2018). To correct the tropospheric disturbances, we used elevation-dependent polynomial approximation (e.g., Cavalié et al., 2007; Wicks et al., 2002) and the Generic Atmospheric Correction Online Service (GACOS) (Yu et al., 2018). Each correction procedure is described in Text S1 of Supporting Information S1. All correction results are compared in Figure S4 of Supporting Information S1. We used the best-corrected result for each interferogram in the slip inversion in Chapter 3.

Table 1
Source Parameters of the Disastrous Earthquakes in Eastern Taiwan That Occurred in 2022

No.	Name	Time (UTC)	Lon (°E)	Lat (°N)	Depth (km)	M_w	Strike (°)	Dip (°)	Rake (°)	Fault
1	Yuli EQ	2022/03/22 17:41:39	121.6118	23.3985	25.73	6.7	16.46	52.72	80.96	LVF
2	Guanshan EQ	2022/09/17 13:41:19	121.1608	23.0840	8.61	6.5	201.45	61.54	15.04	CRF
3	Chihshang EQ	2022/09/18 06:44:15	121.1958	23.1370	7.81	7.0	210.48	56.31	40.38	CRF

Note. Parameters are provided by AutoBATS CMT catalog (IESAST, 1996; Jian et al., 2018).

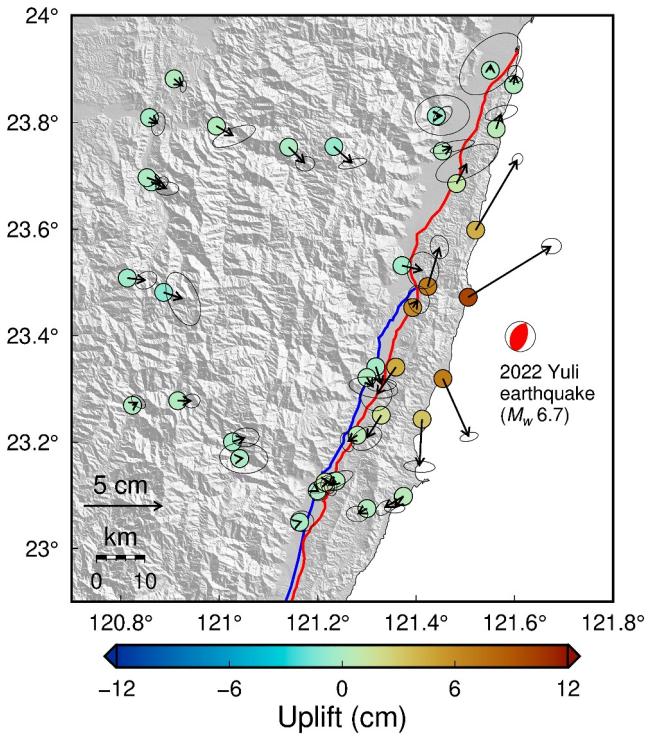

Figure 2. Coseismic displacements at the GNSS stations relative to S01R (23.66°N, 119.59°E). Arrows indicate the horizontal components. Colors of each circle indicate the vertical component. The ellipses display data uncertainty (95% confidence interval) of the horizontal components. Red and blue lines show the surface trace of the LVF and the CRF, respectively. A red beachball denotes the epicenter of the Yuli earthquake.

After subtracting the ionospheric and the tropospheric delays, the spectral enhancement filter (Goldstein & Werner, 1998) was applied with a filter coefficient of 0.4 and a window size of 32 pixels, and unwrapped the interferograms with the minimum cost flow method (Costantini, 1998). To integrate the reference point of InSAR and GNSS, we added a constant offset to each interferogram such that root mean squared error (RMSE) between InSAR and GNSS is minimized considering the GNSS reference station S01R is outside the interferogram.

The four interferograms most consistent with the GNSS data (i.e., most successfully corrected) are shown in Figure 3. All interferograms are in good agreement with GNSS data converted to line-of-sight (LOS) displacement (circles in Figure 3). We can see coseismic deformation around the LVF in all interferograms. The descending right-looking images (Figures 3a and 3b) indicate a remarkable length decrease (negative LOS displacements) to the east of the LVF trace, which is consistent with large uplift and eastward displacements observed by the GNSS (Figure 2). Also, the descending left-looking image (Figure 3c) and the ascending right-looking image (Figure 3d) show the length increase (positive LOS displacement) on the west side of the LVF trace, where only few GNSS stations are available. The sharp gradient in the surface displacements along the LVF trace is clearly visible in these two interferograms. All the above-mentioned features consistently support the rupture of the LVF, and it dips to the east.

3. Coseismic Slip Inversion of the 2022 Yuli Earthquake

In this Chapter, we describe how to estimate the slip distribution on the LVF associated with the Yuli earthquake by a joint inversion using GNSS and InSAR data.

First, we subsampled the four corrected interferograms to reduce the computational cost. The most common method would be the quadtree decomposition (e.g., Abe et al., 2013; Jónsson et al., 2002). In eastern Taiwan, however, this algorithm is not suitable because phase gradients unrelated to earthquakes are distributed heterogeneously in space, resulting in dense sampling even far from the hypocenter. These phase gradients are possibly due to the remnants of the tropospheric noise that correlates with topography. To avoid this problem, we adopted uniform subsampling (e.g., Pritchard et al., 2002) at 3 km intervals and obtained 2,938 points from the four interferograms as indicated in Figure S5 of Supporting Information S1.

We then estimated the fault slip vector **m** by a weighted damped least-squares inversion (Menke, 2018):

$$\mathbf{m} = \left(\mathbf{G}^{t}\mathbf{W}\mathbf{G} + \varepsilon^{2}\mathbf{D}^{t}\mathbf{D}\right)^{-1}\mathbf{G}^{t}\mathbf{W}\mathbf{d}, \quad (1)$$

Table 2
ALOS-2 InSAR Images (ScanSAR) Across the Yuli Earthquake on 22 March 2022

No.	Path	Frame	Orbit[a]	Bandwidth (MHz)	Incidence Angle[b]	Primary	Secondary
1	25	3150	DR	28	58.3°	2021/12/16	2022/05/19
2	27	3150	DR	14	41.5°	2022/03/20	2022/04/03
3	34	3100	DL	28	53.4°	2022/02/27	2022/05/22
4	138	450	AR	28	47.9°	2022/02/15	2022/06/07

[a]DR, descending right looking; DL, descending left looking; AR, ascending right looking. [b]Incidence angle at the center of the study area (23.45°N, 121.25°E).

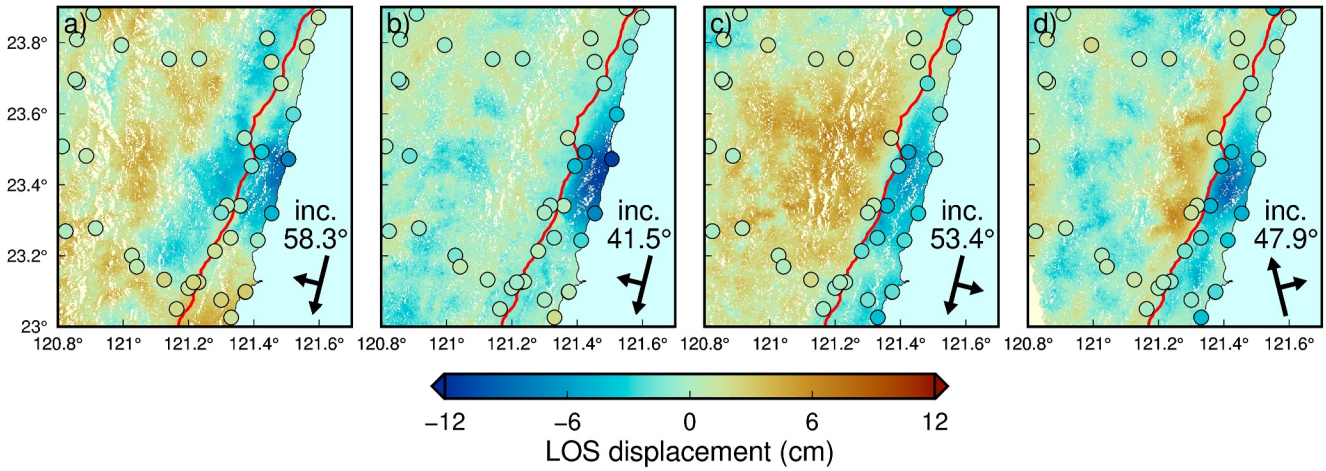

Figure 3. Four corrected interferograms most consistent with the GNSS data. The details are listed in Table 2. (a) Path 25 corrected by SSM and a linear function of elevation. (b) Path 27 corrected by a polynomial and GACOS. (c) Path 34 corrected by SSM and GACOS. (d) Path 138 corrected by SSM and GACOS. Flight and beam directions are indicated by black arrows together with incidence angles. The red line indicates the surface trace of the LVF. Colored circles show LOS displacement derived from the GNSS data. See Figure S4 in Supporting Information S1 for all corrected results.

where **d** is the data vector, **G** is the design matrix which consists of the Green's function for the fault slip in an elastic half-space (Okada, 1985) assuming a Poisson's ratio of 0.25, **W** is the weight matrix, **D** is the Laplacian operator matrix (e.g., Jónsson et al., 2002), and ε^2 is weight of the smoothness constraint.

To generate the matrix **G**, it is necessary to assume the fault geometry. According to the previous study (Lee et al., 2008), the LVF takes a listric shape in the southern segment and a flat shape in other areas including the Yuli earthquake hypocenter. The aftershocks of the Yuli earthquake (Figure 4) also demonstrate that the dip angle is almost constant. Therefore, we approximate the fault geometry as a flat plane (e.g., Lee et al., 2023; Lin, Hsu, & Canitano, 2023; Tang et al., 2025). The dip angle is determined to be 70° down to the east based on the aftershock distribution. We also consider models with different geometries and discuss the optimal dip angle at the end of this chapter.

To consider uncertainty in the observations, the data are weighted using the covariance matrix. Diagonal terms of the GNSS covariance matrix $\mathbf{C}_{\mathrm{GNSS}}$ are determined by the variance of the coseismic displacements calculated from daily coordinates. The standard deviations of the GNSS data are listed in Table S1 of Supporting Information S1. Off-diagonal components of the GNSS covariance matrix are assumed to be zero. Spatially correlated noise of the InSAR is expressed by the covariance matrix $\mathbf{C}_{\mathrm{InSAR}}$ with off-diagonal components (e.g., Fukushima et al., 2005; Lohman & Simons, 2005). Specifically, the i th and j th component of the $\mathbf{C}_{\mathrm{InSAR}}$ can be expressed as

$$(\mathbf{C}_{\mathrm{InSAR}})_{ij} = \sigma^2 \exp\left(-\frac{r_{ij}}{a}\right), \tag{2}$$

where σ^2 is the variance of the InSAR data, r_{ij} stands for the distance between the i th and j th pixels, and a indicates the characteristic length scale. The values of σ^2 and a are assumed to be uniform over the image and common for all paths. We set the correlation length a as 10,000 m, the same value as Lohman and Simons (2005). Following previous studies (e.g., Ghayournajarkar & Fukushima, 2020), we estimated the standard deviation of the InSAR data σ (Table S2 in Supporting Information S1) in the reference area (blue frame in Figure S1 of Supporting Information S1), where coseismic deformation is negligible. Based on this estimation, we roughly assumed the standard deviation of the InSAR to be 1 cm (i.e., σ^2 to be 10^{-4} m^2) for all scenes. Eventually, we defined the covariance matrix **C** as

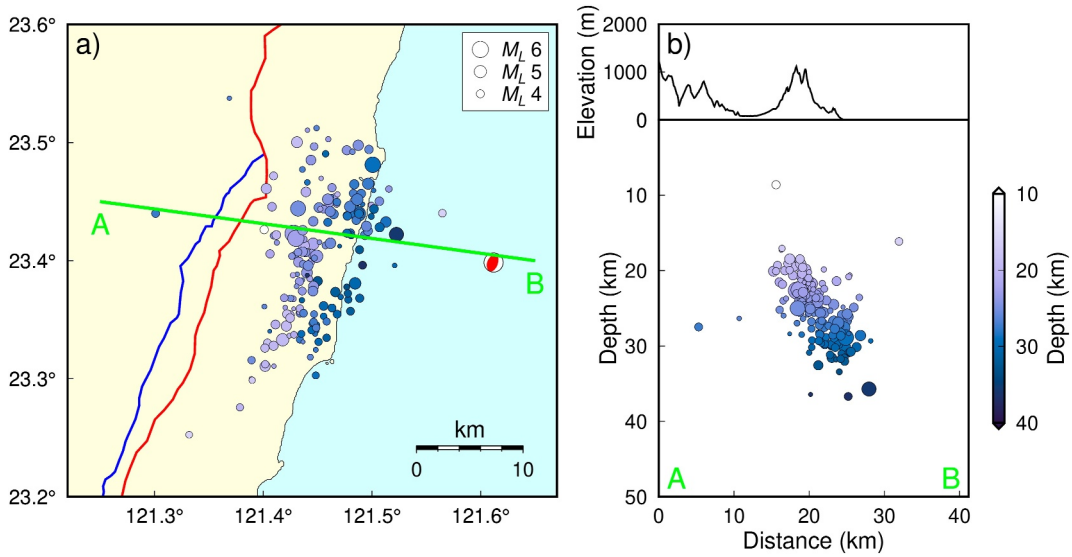

Figure 4. Distribution of $M_L > 3$ aftershocks from 22 to 29 March, 2022 (CWA, 2012). (a) Map view of the aftershocks. Colors of the circles corresponds to the hypocentral depth. Red and blue lines indicate the surface trace of the LVF and the CRF, respectively. A red beach ball indicates the epicenter and the focal solution of the Yuli earthquake. (b) Cross section along A to B in (a). Elevation and aftershocks within 20 km from the line AB were projected.

$$\mathbf{C} = \begin{bmatrix} \mathbf{C}_{\mathrm{GNSS}} & \mathbf{0} & \mathbf{0} & \mathbf{0} & \mathbf{0} \\ \mathbf{0} & \mathbf{C}_{\mathrm{InSAR}_{25}} & \mathbf{0} & \mathbf{0} & \mathbf{0} \\ \mathbf{0} & \mathbf{0} & \mathbf{C}_{\mathrm{InSAR}_{27}} & \mathbf{0} & \mathbf{0} \\ \mathbf{0} & \mathbf{0} & \mathbf{0} & \mathbf{C}_{\mathrm{InSAR}_{34}} & \mathbf{0} \\ \mathbf{0} & \mathbf{0} & \mathbf{0} & \mathbf{0} & \mathbf{C}_{\mathrm{InSAR}_{138}} \end{bmatrix}. \quad (3)$$

The indices of the InSAR covariance matrices indicate the path numbers of interferograms. The weight matrix $\mathbf{W}$ in Equation 1 is defined as follows:

$$\mathbf{W} = \mathbf{C}^{-1}. \quad (4)$$

The optimal weight of the smoothness constraint ε^2 was determined to be 1,000 by the L-curve method (Hansen, 1992; Hansen & O'Leary, 1993) (Figure S6 in Supporting Information S1).

We additionally performed a resolution test of our inversion. First, we input a 50 cm dip-slip within a square-shaped area of 15 km dimension at the deep and shallow portions of the fault (Figures S7a and S7b in Supporting Information S1) and calculated the surface displacements. Next, we inverted the fault slip from the synthetic surface displacements. The results show that the depth resolution is sufficient to reconstruct the hypothetical slip, although the resolution is poorer as we go deeper (Figures S7c and S7d in Supporting Information S1).

The estimated slip distribution of the Yuli earthquake (Figure 5) predominantly indicates reverse faulting, which is consistent with the focal solution (Figure 1). Note that the centroid location of the AutoBATS CMT solution is displaced offshore due to estimation uncertainty. The main rupture concentrated at the depth range of 10–30 km with a maximum slip of 50 cm (Figure 5), while shallow part of the fault did not slip during the earthquake. The moment magnitude (Kanamori, 1977) is 6.7 assuming a rigidity of 40 GPa, which is equivalent to the AutoBATS CMT catalog (Table 1). The large slip area on the fault plane corresponds to the hypocenters of aftershocks (Figure 6). The trend of overlapping slip area and aftershocks is also observed in the 2003 Chengkung earthquake in the southern part of the LVF (e.g., Ching et al., 2007). The surface displacements calculated from the estimated slip well explain the observations (Figure 7).

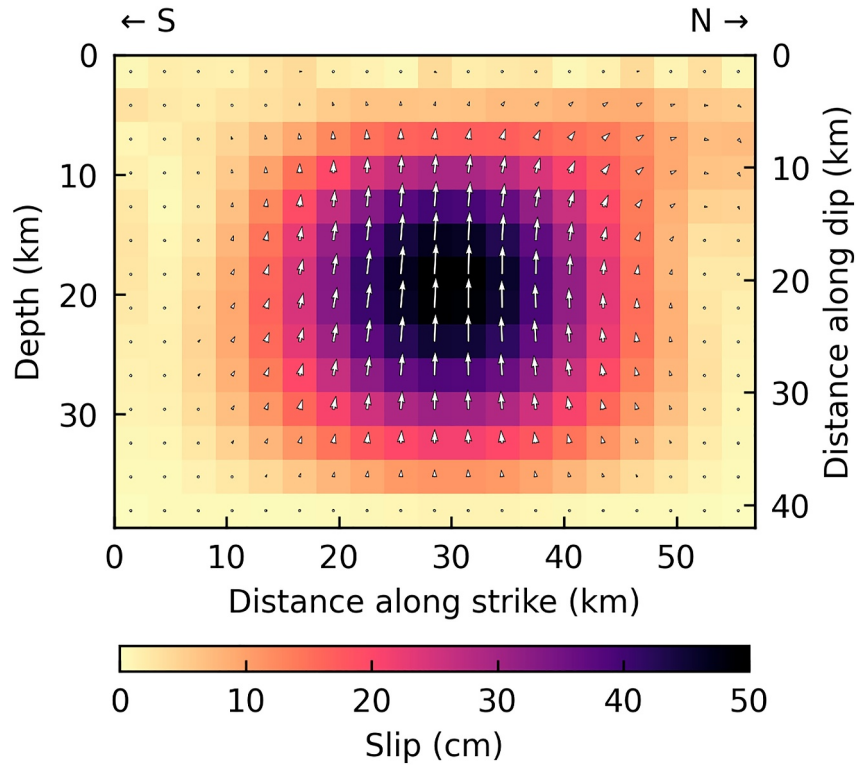

Figure 5. Optimal coseismic slip distribution of the Yuli earthquake. Dip angle is set to 70°. Colors show the slip magnitude. White arrows indicate the slip vectors.

In addition to Figure 7, we searched the optimal fault geometry using a planar fault with different dip angles (50°, 60°, and 80°) (Figures S8–S10 in Supporting Information S1), as well as a listric shape with the dip angle varying from 75° to 45° from surface to depth (Shyu et al., 2020; Tang et al., 2023) (Figure S11 in Supporting Information S1). As a result, we concluded that the planar geometry dipping at 70° is optimal, based on the RMSEs for each case (Table S3 in Supporting Information S1). In particular, the residual of the GNSS data for the case of 70° (Figure 7) is smaller than the others (Figure S8–S11 in Supporting Information S1). Furthermore, the plane dipping at 70° aligns well with the aftershock distribution (Figure 4b), while the listric geometry is not consistent with it. Therefore, we suggest that the LVF around the Yuli earthquake rupture is almost planar, which is also supported by the relocated 3-D seismicity distribution in this area (Lee et al., 2008).

4. Effect on the 2022 Chihshang Earthquake

We quantitatively evaluate the effect of the Yuli earthquake on the Chihshang earthquake (M_w 7.0) that occurred on the CRF in September 2022, about 6 months later. The Chihshang earthquake occurred on the west-dipping CRF along the western edge of the Longitudinal Valley (Figure 1) (He et al., 2024; Lee et al., 2023; Tang et al., 2023; Tung et al., 2025; Yagi et al., 2023; Yang et al., 2024). Previous studies commonly suggest that the rupture propagated significantly to the north of its hypocenter (green contours in Figure 8). The hypocenter of the Yuli earthquake is located close to the northern part of the rupture area of the Chihshang earthquake (Figure 8).

4.1. Stress Change on the CRF Caused by the Yuli Earthquake

To quantify the stress perturbation on the CRF caused by the Yuli earthquake on the LVF, we calculated changes in Coulomb failure function (ΔCFF) (e.g., King et al., 1994; Reasenberg & Simpson, 1992; Stein, 1999) using Coulomb 3.3 package (Toda et al., 2011). The ΔCFF is defined as

$$\Delta \mathrm{CFF} = \Delta\tau - \mu' \Delta\sigma, \tag{5}$$

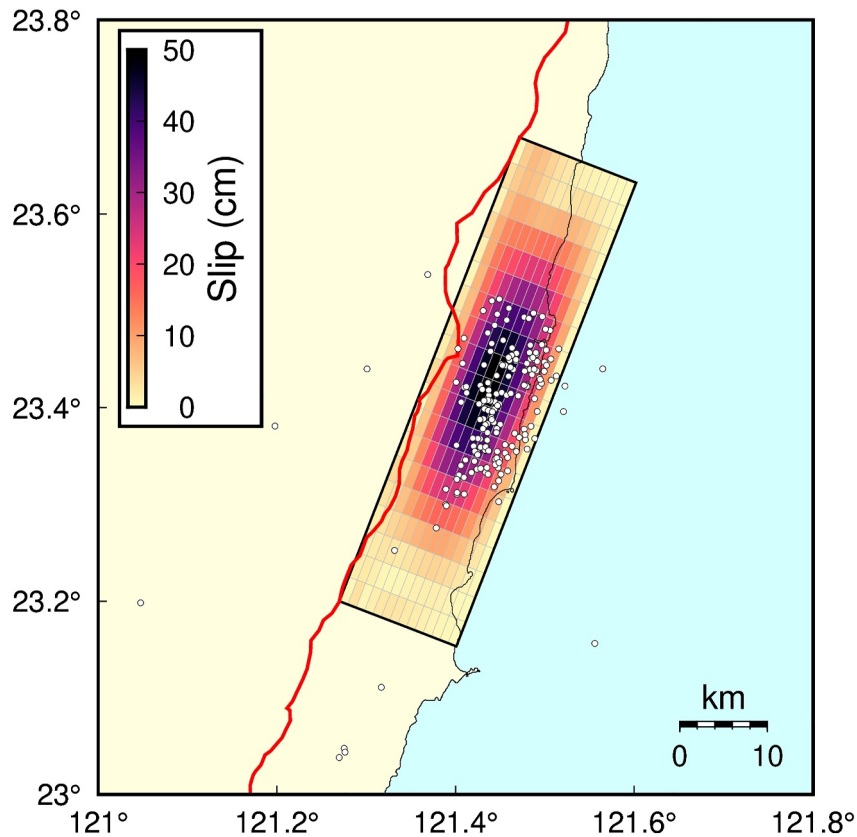

Figure 6. Map view of the estimated fault slip and aftershocks. White dots are aftershocks of $M_L > 3$ from 22 to 29 March, 2022 (CWA, 2012). A red line represents the fault trace of the LVF.

where $\Delta\tau$ is the shear stress change in the slip direction on the receiver fault, $\Delta\sigma$ is the normal stress change on the receiver fault (positive in compression), and μ' is the apparent friction coefficient, considering changes in pore pressure. Failure is encouraged when ΔCFF is positive and discouraged when negative. In other words, shear stress increase or unclamping promotes the fault rupture. We assumed the apparent friction coefficient μ' of 0.4 (Hsu et al., 2010; Tang et al., 2023), a rigidity of 40 GPa, and a Poisson's ratio of 0.25. The fault geometry and slip rake angle of the CRF were taken from Tang et al. (2023).

The result shows a positive ΔCFF of about 0.25 MPa in the northern portion of the main rupture area of the Chihshang earthquake (Figure 8a), which led to slight increases in aftershocks there. The positive ΔCFF appears with the contribution of both the shear stress change and the normal stress change (Figure S12 in Supporting Information S1). To elaborate on the effect of the apparent friction μ', we calculated the ΔCFF by changing it. Although the ΔCFF increases almost proportionally with μ', the overall pattern remains largely unchanged (Figure S13 in Supporting Information S1). Considering that the hypocenter of the Chihshang earthquake is located at the southern tip of the main rupture area (Figure 8a), the stress increase due to the Yuli earthquake should have helped northward rupture propagation of the Chihshang earthquake.

In this study, we focused on the correspondence between the spatial distribution of the positive ΔCFF due to the Yuli earthquake and the rupture area of the Chihshang earthquake. On the other hand, the key aspect of ΔCFF interpretation in recent studies is its influence on rupture nucleation and immediate excitation of seismicity (e.g., Dieterich, 1994; Stein, 1999). Once the fault rupture begins, it propagates dynamically on its own. While the ΔCFF caused by the Yuli earthquake is expected to have an important effect on the rupture propagation of the Chihshang earthquake, we recognize that the dynamic effects of the Chihshang earthquake play a major role, which should be explored in the future.

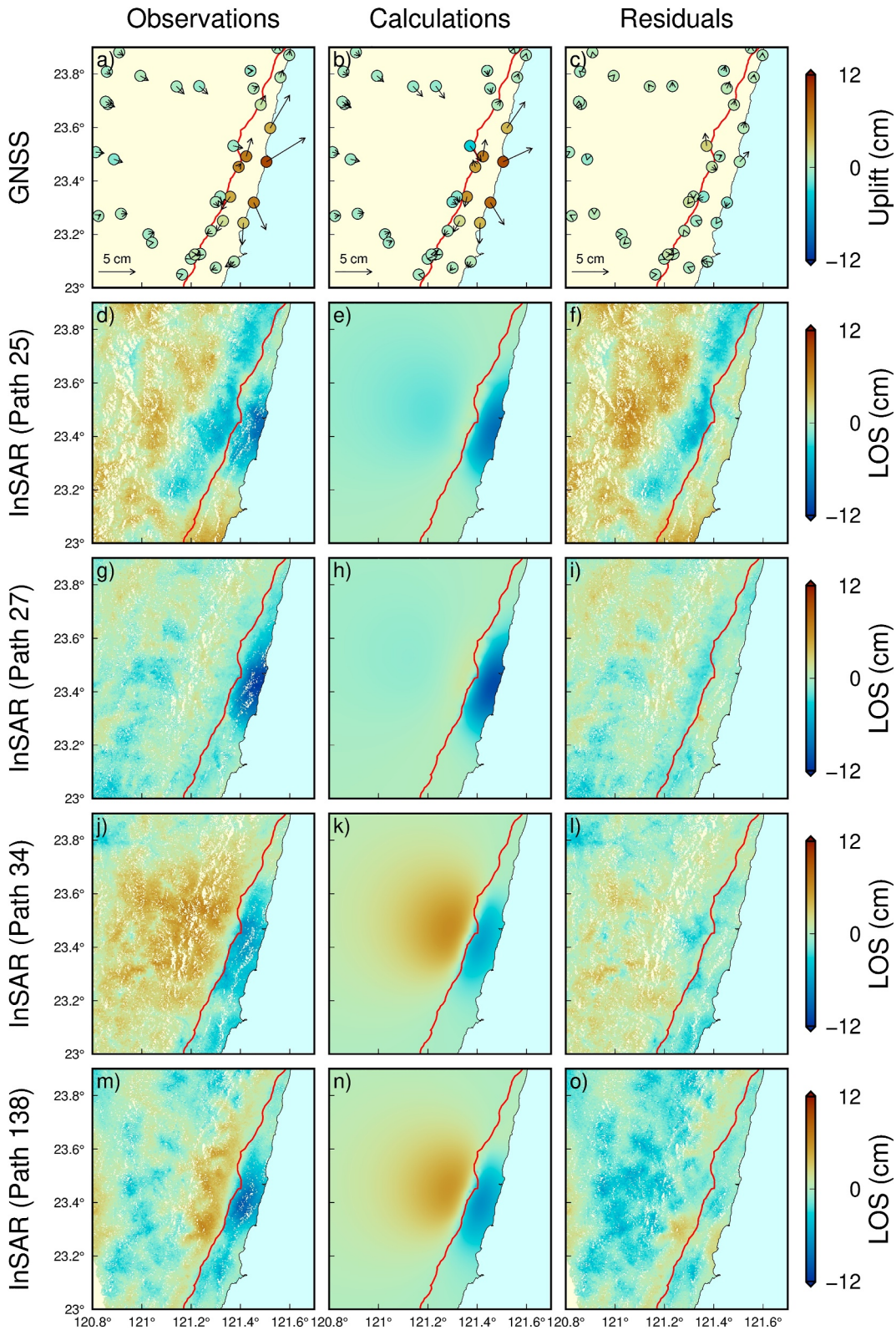

Figure 7. Comparison between the observations (left), the synthetic data derived from the optimal fault slip (Figure 5) (center), and the residuals (right). (a–c) GNSS. Colors indicate the vertical displacement. (d–f) Interferogram of Path 25 (DR). (g–i) Path 27 (DR). (j–l) Path 34 (DL). (m–o) Path 138 (AR).

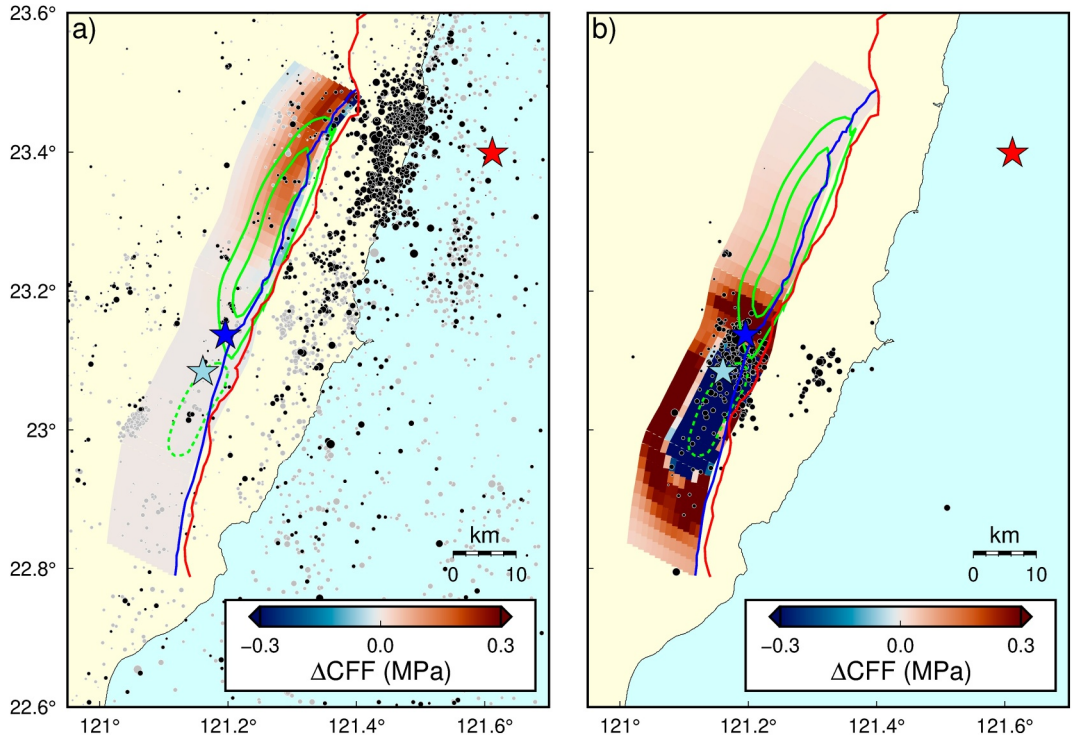

Figure 8. (a) Changes in coulomb failure function (ΔCFF) on the CRF associated with the 2022 Yuli earthquake. Gray circles indicate 1-year seismicity before the Yuli earthquake. Black circles are aftershocks between the Yuli earthquake and the Guanshan earthquake. (b) The ΔCFF on the CRF associated with the 2022 Guanshan earthquake. We used the coseismic slip model of the Guanshan earthquake estimated by Tang et al. (2023). Black circles are aftershocks between the Guanshan earthquake and the Chihshang earthquake. We set the rake angle of the CRF to 45° (Tang et al., 2023). The apparent friction coefficient μ' is assumed to be 0.4. Red, light blue, and blue stars indicate the epicenter of the Yuli earthquake, the Guanshan earthquake, and the Chihshang earthquake, respectively. Red and blue lines indicate the surface trace of the LVF and the CRF, respectively. The green contours show the coseismic slip distribution of the Guanshan earthquake (dashed, every 50 cm) and the Chihshang earthquake (solid, every 100 cm) estimated by Tang et al. (2023). The ΔCFF caused by the Yuli earthquake is predominantly positive over a wide area on the CRF, reaching more than 0.25 MPa in the northern part of the main shock area.

4.2. Role of the Guanshan Earthquake

The M_w 6.5 Guanshan earthquake, a foreshock of the Chihshang earthquake, struck just south of the Chihshang earthquake's hypocenter 17 hr earlier (light blue star in Figure 8). In this section, we discuss the role of the Guanshan earthquake in the three successive earthquakes by elaborating on the ΔCFF and the aftershocks in chronological order. First, we discuss the impact of the Yuli earthquake on the Guanshan earthquake. The ΔCFF at the hypocenter of the Guanshan earthquake is negligible (<0.01 MPa), where no significant seismicity increase was observed (Figure 8a). Therefore, it is less likely that the Guanshan earthquake was triggered by the Yuli earthquake. Next, we calculated the ΔCFF on the CRF due to the Guanshan earthquake to examine its effect on the Chihshang earthquake. We obtained the positive ΔCFF up to 0.93 MPa at the hypocentral area of the Chihshang earthquake located in the southern tip of the rupture area, which led to intensive aftershocks, including the occurrence of the Chihshang earthquake (Figure 8b). Thus, it is clear that the Guanshan earthquake triggered the Chihshang earthquake. However, the area with positive ΔCFF is spatially limited compared to the positive ΔCFF caused by the Yuli earthquake (Figure 8b). Note that the ΔCFF due to the Guanshan earthquake does not reach 0.05 MPa in the north of 23.3°N corresponding to the northern half of the rupture area of the Chihshang earthquake. Therefore, we propose that the Guanshan earthquake triggered the Chihshang earthquake and the Yuli earthquake promoted its northward rupture propagation.

4.3. Clock Advance Caused by the Yuli Earthquake

To further quantify the effect of the Yuli earthquake on the Chihshang earthquake, we calculated the "clock advance" (e.g., Harris & Simpson, 1992; King et al., 1994). The clock advance Δt is defined as

$$\Delta t = \frac{\Delta \mathrm{CFF}}{\dot{\mathrm{CFF}}}, \tag{6}$$

where $\dot{\mathrm{CFF}}$ is the long-term stressing rate on the rupture area of the Chihshang earthquake. It means how long it takes to accumulate stress equivalent to the stress change caused by the Yuli earthquake. We can roughly estimate the long-term stressing rate $\dot{\mathrm{CFF}}$ at the coseismic rupture area of the Chihshang earthquake by assigning steady fault slip on the deeper extension of both the CRF and the LVF (e.g., Harris & Simpson, 1992). To execute this estimation, we adopted the concept of a back-slip model (Savage, 1983). With Green's function of the elastic half-space (Okada, 1992), the long-term stress accumulation on the rupture area of the Chihshang earthquake can be calculated by imposing a hypothetical slip there in the direction opposite to the long-term slip of the CRF. The same procedure is applied to the LVF. We assumed the long-term slip rate of the CRF as 10 mm/yr considering that the late Quaternary slip rate of the CRF has been estimated to be less than 12.8 mm/yr (Shyu, Sieh, Chen, & Chung, 2006). We set the rake angle of both faults as 45° (Tang et al., 2023). We also set the dip angle and the long-term slip rate of the LVF as 70° (our optimal model) and 10 mm/yr (Shyu et al., 2020), respectively. The locking depth is ranging 20–40 km to account for the uncertainty in the seismogenic layer thickness in this region (Lee et al., 2008).

Following the above procedure, we obtained the long-term stressing rate on the Chihshang earthquake rupture area (6 km depth) as 0.0069 and 0.0025 MPa/yr when the locking depth is set to 20 and 40 km, respectively. Considering the ΔCFF due to the Yuli earthquake as ~0.25 MPa (Figure 8a), the clock advance estimated from Equation 6 is 36 years when the locking depth is 20 km. When the locking depth changes to 40 km, the clock advance becomes 100 years. Although it is a rough estimate, the stress change due to the Yuli earthquake is equivalent to 36–100 years of steady stress accumulation in the rupture area of the Chihshang earthquake, which suggests a large impact on the earthquake generation cycles. As a reference, a comparable value (<56 years) has been estimated for a segment of the San Andreas fault system due to the 1992 Landers earthquake (M 7.4) (Stein et al., 1992).

5. Fault Interaction in Double-Vergence Structure

In Chapter 4, we proposed that the Yuli earthquake on the LVF promoted the northward rupture propagation of the Chihshang earthquake on the CRF. In contrast, Tang et al. (2023) suggested that an earthquake on either the LVF or CRF suppresses the seismicity on the other fault based on the historical earthquake catalog ($M > 6$) and the ΔCFF calculation. To explain these seemingly contradictory findings, in this chapter, we provide a comprehensive framework for the kinematic interaction between the LVF and the CRF by focusing on the effect of rake angles.

5.1. Effect of Rake Angle in Stress Change Calculation

Let us check the rake angles of the major earthquakes occurred on the LVF and the CRF. Tang et al. (2023) showed that both the 1951 Longitudinal Valley earthquake sequence on the LVF and the 2022 Chihshang earthquake on the CRF caused negative ΔCFF on the other fault. The rake angles of these earthquakes are both close to 45° or less (Chung et al., 2008; Lee et al., 2008; Tang et al., 2023). On the other hand, the rake angle of the Yuli earthquake on the LVF that caused the positive ΔCFF on the CRF (Figure 8a) is close to 90° (Figure 5). We therefore hypothesize that the difference in ΔCFF on the receiver fault of this double-vergence fault system is largely attributed to the rake angle variation of the fault slip on the source fault.

To obtain a more general understanding of the rake angle dependency, we performed a numerical calculation. For simplicity and to ensure generality, we consider a pair of symmetrical faults with a dip angle of 70°, corresponding to the LVF and the CRF (Figure 9a). On the source fault (LVF), we set a Gaussian-shaped slip distribution of uniform rake angle with a maximum slip of 50 cm (Figure 9b), which is comparable to the Yuli earthquake, and systematically changed the rake angle from 90° to 0°. On the receiver fault (CRF), the rake angle is fixed to be 45°, which is the case of the Chihshang earthquake (Tang et al., 2023). Since the two faults are symmetric (Figure 9a), the opposite case (i.e., an earthquake on the CRF changes the stress on the LVF) yields the same result. Even in the opposite case, it is reasonable to set the rake angle of the receiver fault (LVF) to 45° because the LVF has consumed the horizontal convergence in a southeast-northwest direction in the long term

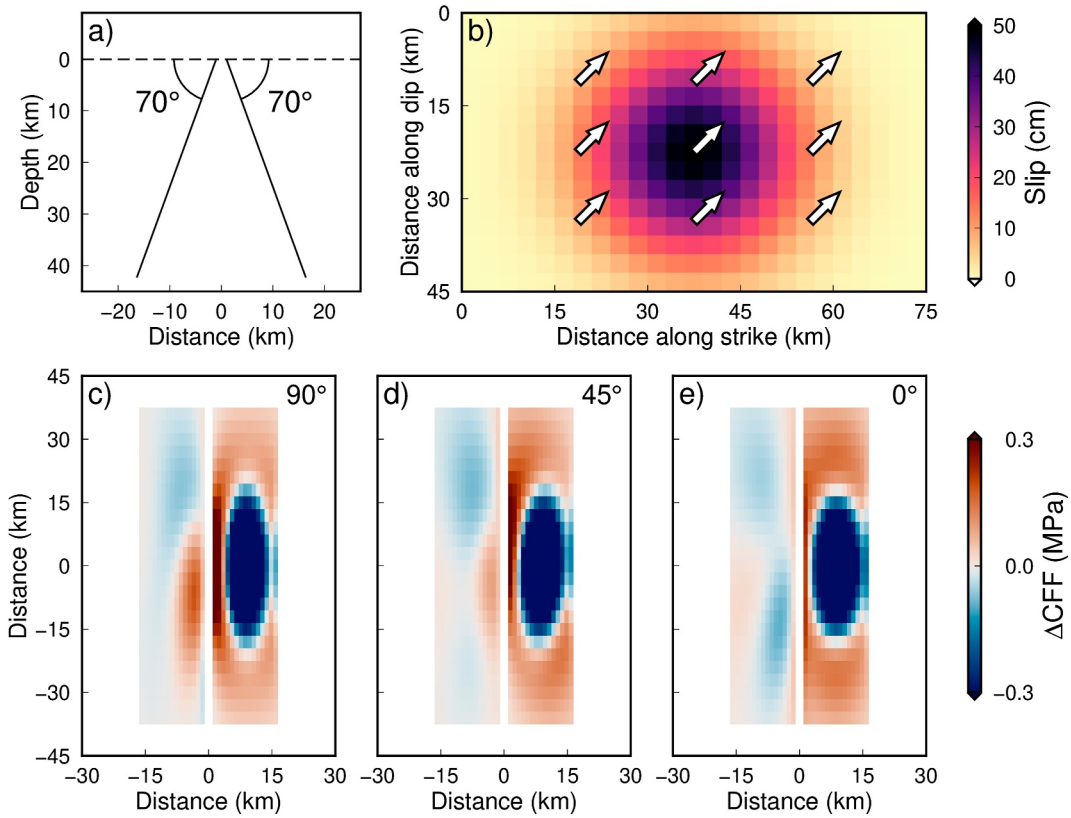

Figure 9. A simple model for the fault interaction of a double-vergence fault system. (a) Cross section of the fault system. Both faults dip outward at 70°. (b) Gaussian-shaped distribution used for the slip of the source fault. We systematically change its rake angles from 90° to 0°. The rake angles are spatially uniform in each case (this is the case of 45°). (c–e) Changes in Coulomb failure function (ΔCFF) on a receiver fault (left) caused by a fault slip of variable rake angles on the source fault (right). The rake angles of the source fault are (c) 90°, (d) 45°, and (e) 0°. The rake angle of the receiver fault is fixed to be 45°. Strong positive ΔCFF appears broadly on the receiver fault when the rake angle of the source fault is 90°, while negative values are dominant when the rake angle is less than 45°.

(e.g., Lee et al., 2008), which makes rake angle of 45° typical for earthquakes on the LVF (e.g., Hsu, Yu, Simons, et al., 2009; Wu et al., 2008).

The ΔCFF on the CRF caused by the fault slip on the LVF with variable rake angles is shown in Figures 9c–9e. When the rake angle is 90°, the ΔCFF on the CRF is dominated by the large positive value approaching 0.2 MPa (Figure 9c). When the rake angle is 45° or 0°, ΔCFF on the CRF mainly shows a negative value (Figures 9d and 9e). Thus, the contrasting results of the previous study (Tang et al., 2023) and ours, that is, (a) fault slips on one fault suppress the earthquakes on the other, and (b) the 2022 Yuli earthquake on the LVF caused positive ΔCFF on the CRF, can be comprehensively understood as the systematic behavior of the double-vergence fault system in response to the different rake angle of the source fault.

In Figure 9, we set the rake angle of the receiver fault to 45° considering the long-term convergence direction across the LVF and the CRF, which is also consistent with the rake angle of large earthquakes like the 1951 earthquake and the 2022 Chihshang earthquake. Note that a pure dip-slip on the source fault always causes the largest ΔCFF on the receiver fault even if the receiver fault takes various rake angles ranging from 0° to 90° (Figure S14 in Supporting Information S1).

Additionally, we examined the influence of slip depth on the source fault. We calculated the ΔCFF by shifting the input slip (Figure 9b) 15 km shallower and deeper along the dip direction (depth of 7.0 and 35.2 km, respectively). When the slip is shallower (rupture to the surface), the stress changes on the receiver fault shift shallower overall (Figure S15 in Supporting Information S1). When the slip is deeper, they shift deeper (Figure S16 in Supporting Information S1). Specifically, a pure dip-slip at a depth of 7.0 km causes the greatest increase in ΔCFF on the

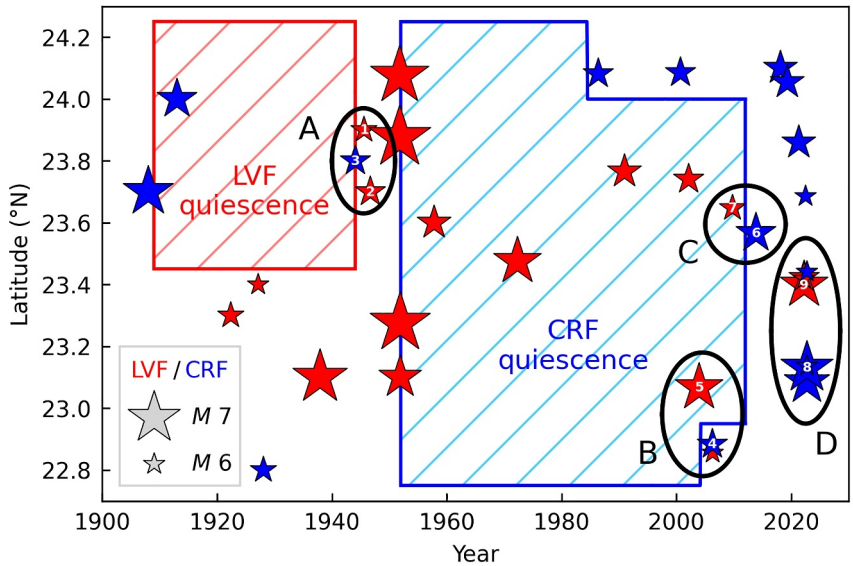

Figure 10. Spatiotemporal distribution of earthquakes on the LVF and the CRF since 1900 with $M > 6$ and depth <30 km (modified from Tang et al. (2023)). Red and blue stars represent the earthquakes occurred on the LVF and the CRF, respectively. The frames filled in red and blue indicate the seismic quiescences proposed by Tang et al. (2023). Black circles from A to D show the earthquake generation on one fault shortly after the earthquake on the other fault. Events labeled with numbers are referenced in the main text.

other fault at 1.4 km depth when the receiver rake is 45° (Figure S15f in Supporting Information S1). Likewise, a dip-slip at a depth of 35.2 km causes the greatest increase in ΔCFF on the other fault at 15.5 km depth (Figure S16f in Supporting Information S1). These results clearly indicate that the slip depth does not affect the rake angle dependency of ΔCFF on the receiver fault.

5.2. Reassessment of Historical Seismicity

We further assess the historical earthquake record along the LVF and the CRF based on the rake angle dependency of the ΔCFF. Figure 10 displays the spatiotemporal distribution of historical seismicity in eastern Taiwan since 1900 with magnitudes larger than 6 and depths shallower than 30 km. The responsible faults and the magnitudes in this figure are based on Tang et al. (2023).

According to Tang et al. (2023), seismicity quiescence has been observed twice in eastern Taiwan since 1900 (red and blue frames in Figure 10): a 37-year-long quiescence on the LVF after the 1908 earthquake on the CRF, and a 62-year-long quiescence on the CRF after the 1951 Longitudinal Valley earthquake sequence on the LVF. The rake angle of the 1908 earthquake is unknown, while that of the 1951 earthquake sequence is mainly less than 45° (Chung et al., 2008; Lee et al., 2008). Therefore, based on our numerical calculations with rake angles of 45° (Figure 9d) and 0° (Figure 9e), we can interpret that the negative ΔCFF caused by the 1951 earthquake sequence on the LVF results in the 62-year-long quiescence on the CRF. In addition, a numerical calculation by Tang et al. (2023) shows that the 1951 earthquake on the LVF caused a negative ΔCFF on the CRF, which is consistent with our calculations.

On the other hand, we can find that earthquakes occurred on one fault shortly after the earthquake on the other fault as indicated by circles A–D in Figure 10. In case A, two earthquakes occurred on the LVF in 1945 and 1946 (stars No. 1 and 2 in Figure 10), just after the 1943–1944 Hualien earthquake sequence on the CRF (star No. 3 in Figure 10). In case B, the 2006 Taitung earthquake occurred on the CRF (Mozziconacci et al., 2013; Wu, Chen, Chang, et al., 2006) (star No. 4 in Figure 10) after the 2003 Chengkung earthquake on the LVF (Ching et al., 2007; Hsu, Yu, & Chen, 2009; Wu, Chen, Shin, et al., 2006) (star No. 5 in Figure 10). In case C, the 2013 Ruisui earthquake occurred on the CRF (Canitano et al., 2015; Lee et al., 2014; Lin, Gualandi, et al., 2023) (star No. 6 in Figure 10), after the 2009 Fengpin earthquake on the LVF (Lin, Hsu, & Canitano, 2023) (star No. 7 in Figure 10). Finally, in case D, the 2022 Chihshang earthquake on the CRF (star No. 8 in Figure 10) occurred 6 months after the Yuli earthquake on the LVF (this paper) (star No. 9 in Figure 10).

Next, we elaborate on the rake angles of the first earthquakes (i.e., source) in cases B and C (Figure 10). Note that we know the rake angle of case D (Figure 5) and no reliable data have been found for case A (too old). In case B, the rake angle of the 2003 Chengkung earthquake was about 90° (Ching et al., 2007; Hsu, Yu, & Chen, 2009; Wu, Chen, Shin, et al., 2006). Indeed, Wu, Chen, Chang, et al. (2006) suggested that the Chengkung earthquake on the LVF caused a positive ΔCFF on the CRF, which is consistent with our calculation (Figure 9c). In case C, the 2009 Fengpin earthquake also had a rake angle greater than 45° (Lin, Hsu, & Canitano, 2023) and therefore we can expect a positive ΔCFF on the CRF based on our calculation (Figure 9c). As we mentioned above, the opposite cases can also be explained in the same way: the rake angles smaller than 45° for the 1951 Longitudinal Valley earthquake sequence and the 2022 Chihshang earthquake led to the seismicity quiescence on the other fault. Thus, both the promotion and the suppression of seismicity due to the kinematic interaction of the double-vergence faults can be explained by differences in the rake angle of the fault slip as indicated in Figure 9.

It should be noted that case A–D in Figure 10 occurred at the ends of seismicity quiescences. This feature emphasizes that the stress build-up on the fault plane is the prerequisite for earthquake generation. A precise expression of our finding is, therefore, when one fault in the double-vergence system is "well-prepared", a dip-slip earthquake on the other fault highly promotes the earthquake generation.

Based on our findings, we demonstrated the importance of precise rake angle estimation for the seismic risk assessment. In eastern Taiwan, more widespread and continuous observations should improve the estimation accuracy, which can be achieved by the deployment of ocean bottom seismometers (e.g., Lin et al., 2024), GNSS/Acoustic (e.g., Chen et al., 2018), and future L-band SAR missions such as ALOS-4 and NASA-ISRO SAR Mission (NISAR).

6. Conclusions

In this paper, based on the geodetic inversion and a series of theoretical models, we demonstrated the large impact of the rake angle of fault slip on the kinematic interaction between the CRF and the LVF, an active double-vergence fault system. The kinematic interaction within this fault system had been poorly understood, which manifests itself as the seemingly contradictory behaviors: (a) fault slip on one of these faults leads to the seismicity quiescence on the other fault, (b) the 2022 Chihshang earthquake on the CRF occurred soon after the 2022 Yuli earthquake on the LVF. To comprehensively understand these behaviors, first, we estimated the coseismic slip distribution of the Yuli earthquake by a joint inversion using InSAR and GNSS. The estimated slip distribution indicates almost pure reverse faulting. With this result, we found that the ΔCFF due to the Yuli earthquake reaches +0.25 MPa around the main rupture area of the Chihshang earthquake, which is equivalent to 36–100 years of steady stress accumulation. Thus, we demonstrated that mutual interaction between the LVF and the CRF greatly perturbs the earthquake generation cycles on those faults. Finally, we found that a rake angle of fault slip has a significant effect on the ΔCFF on the other fault in the double-vergence structure; the ΔCFF takes large positive values when the rake angle of the source is almost 90° like the Yuli earthquake, but the negative ΔCFF is dominant when the rake angle is less than 45° like the Chihshang earthquake. Furthermore, the seismicity quiescence and enhancement recorded in the historical catalog are consistent with the above-mentioned effect of the rake angle. In general, an earthquake with a large dip-slip component promotes the seismicity on the other fault in the double-vergence structure, which is very useful knowledge for seismic risk assessment.

Data Availability Statement

ALOS-2 Open and Free data (PALSAR-2 ScanSAR L1.1) is now publicly available at JAXA G-Portal via https://gportal.jaxa.jp/gpr/. The InSAR analysis was performed by GAMMA Software (Wegmüller & Werner, 1997). ASTER GDEM Version 3 (Abrams et al., 2020) is available at https://www.tellusxdp.com/en-us/catalog/data/aster_gdem_ver_3.html. Seismicity catalog in Taiwan is accessible at the Geophysical Database Management System (GDMS) (CWA, 2012) via https://gdms.cwa.gov.tw/catalogDownload.php. The moment magnitudes and focal mechanisms are provided by AutoBATS CMT catalog (IESAST, 1996; Jian et al., 2018) available at https://tecdc.earth.sinica.edu.tw/FM/AutoBATS/. Coulomb 3.3 package (Toda et al., 2011) can be downloaded at https://temblor.net/coulomb/. Figures were created using GMT version 6.4.0 (Wessel et al., 2019; https://www.generic-mapping-tools.org/), PyGMT version 0.13.0 (Uieda et al., 2021; https://www.pygmt.org/), and Matplotlib version 3.8.3 (Hunter, 2007; https://matplotlib.org/). The coseismic displacements of GNSS and InSAR,

and the slip distribution of the Yuli earthquake are available at https://doi.org/10.5281/zenodo.15287084 (Ishimaru et al., 2025).

Acknowledgments
This study was supported by the Japan Society for Promotion of Science KAKENHI 17K05622, 22K03770, and ERI JURP 2024-B-02 in Earthquake Research Institute, the University of Tokyo. The author Yuri Ishimaru received the Seto Prize of the Geodetic Society of Japan and this study was supported by the award. PALSAR-2 Level 1.1 data are shared among PIXEL (PALSAR Interferometry Consortium to Study our Evolving Land surface), and provided from JAXA under a cooperative research contract with PIXEL. We acknowledge the two anonymous reviewers, the associate editor, and the editor, Satoshi Ide, for their helpful comments and suggestions.

References

Abe, T., Furuya, M., & Takada, Y. (2013). Nonplanar Fault source modeling of the 2008 M_w 6.9 Iwate–Miyagi Inland earthquake in Northeast Japan. *Bulletin of the Seismological Society of America*, *103*(1), 507–518. https://doi.org/10.1785/0120120133

Abrams, M., Crippen, R., & Fujisada, H. (2020). ASTER Global Digital Elevation Model (GDEM) and ASTER Global Water Body Dataset (ASTWBD). *Remote Sensing*, *12*(7), 1156. https://doi.org/10.3390/rs12071156

Altamimi, Z., Rebischung, P., Métivier, L., & Collilieux, X. (2016). ITRF2014: A new release of the international terrestrial reference frame modeling nonlinear station motions. *Journal of Geophysical Research: Solid Earth*, *121*(8), 6109–6131. https://doi.org/10.1002/2016JB013098

Angelier, J., Chu, H.-T., & Lee, J.-C. (1997). Shear concentration in a collision zone: Kinematics of the Chihshang fault as revealed by outcrop-scale quantification of active faulting, Longitudinal Valley, eastern Taiwan. *Tectonophysics*, *274*(1–3), 117–143. https://doi.org/10.1016/S0040-1951(96)00301-0

Berryman, K. R., Cochran, U. A., Clark, K. J., Biasi, G. P., Langridge, R. M., & Villamor, P. (2012). Major earthquakes Occur regularly on an isolated plate boundary fault. *Science*, *336*(6089), 1690–1693. https://doi.org/10.1126/science.1218959

Bertiger, W., Bar-Sever, Y., Dorsey, A., Haines, B., Harvey, N., Hemberger, D., et al. (2020). GipsyX/RTGx, a new tool set for space geodetic operations and research. *Advances in Space Research*, *66*(3), 469–489. https://doi.org/10.1016/j.asr.2020.04.015

Brcic, R., Parizzi, A., Eineder, M., Bamler, R., & Meyer, F. (2010). Estimation and compensation of ionospheric delay for SAR interferometry. 2010. *IEEE International Geoscience and Remote Sensing Symposium*, 2908–2911. https://doi.org/10.1109/IGARSS.2010.5652231

Canitano, A., Hsu, Y.-J., Lee, H.-M., Linde, A. T., & Sacks, S. (2015). Near-field strain observations of the October 2013 Ruisui, Taiwan, earthquake: Source parameters and limits of very short-term strain detection. *Earth Planets and Space*, *67*(1), 125. https://doi.org/10.1186/s40623-015-0284-1

Cavalié, O., Doin, M. P., Lasserre, C., & Briole, P. (2007). Ground motion measurement in the Lake Mead area, Nevada, by differential synthetic aperture radar interferometry time series analysis: Probing the lithosphere rheological structure. *Journal of Geophysical Research*, *112*(B3), B03403. https://doi.org/10.1029/2006JB004344

Central Weather Administration. (2012). Central weather administration seismographic network [Dataset]. *International Federation of Digital Seismograph Networks*. https://doi.org/10.7914/SN/T5

Chai, B. H. T. (1972). Structure and tectonic evolution of Taiwan. *American Journal of Science*, *272*(5), 389–432. https://doi.org/10.2475/ajs.272.5.389

Chen, H.-Y., Ikuta, R., Lin, C.-H., Hsu, Y.-J., Kohmi, T., Wang, C.-C., et al. (2018). Back-Arc opening in the western end of the Okinawa trough revealed from GNSS/Acoustic measurements. *Geophysical Research Letters*, *45*(1), 137–145. https://doi.org/10.1002/2017GL075724

Ching, K.-E., Rau, R.-J., & Zeng, Y. (2007). Coseismic source model of the 2003 M_w 6.8 Chengkung earthquake, Taiwan, determined from GPS measurements. *Journal of Geophysical Research*, *112*(B6), B06422. https://doi.org/10.1029/2006JB004439

Chung, L.-H., Chen, Y.-G., Wu, Y.-M., Shyu, J. B. H., Kuo, Y.-T., & Lin, Y.-N. N. (2008). Seismogenic faults along the major suture of the plate boundary deduced by dislocation modeling of Coseismic displacements of the 1951 $M_{7.3}$ Hualien–Taitung earthquake sequence in eastern Taiwan. *Earth and Planetary Science Letters*, *269*(3–4), 416–426. https://doi.org/10.1016/j.epsl.2008.02.035

Costantini, M. (1998). A novel phase unwrapping method based on network programming. *IEEE Transactions on Geoscience and Remote Sensing*, *36*(3), 813–821. https://doi.org/10.1109/36.673674

Dieterich, J. (1994). A constitutive law for rate of earthquake production and its application to earthquake clustering. *Journal of Geophysical Research*, *99*(B2), 2601–2618. https://doi.org/10.1029/93JB02581

Freed, A. M. (2005). Earthquake triggering by static, dynamic, and postseismic stress transfer. *Annual Review of Earth and Planetary Sciences*, *33*(1), 335–367. https://doi.org/10.1146/annurev.earth.33.092203.122505

Fukushima, Y., Cayol, V., & Durand, P. (2005). Finding realistic dike models from interferometric synthetic aperture radar data: The February 2000 eruption at Piton de la Fournaise. *Journal of Geophysical Research*, *110*(B3), B03206. https://doi.org/10.1029/2004JB003268

Fukushima, Y., Toda, S., Miura, S., Ishimura, D., Fukuda, J., Demachi, T., & Tachibana, K. (2018). Extremely early recurrence of intraplate fault rupture following the Tohoku-Oki earthquake. *Nature Geoscience*, *11*(10), 777–781. https://doi.org/10.1038/s41561-018-0201-x

Furuya, M., Suzuki, T., Maeda, J., & Heki, K. (2017). Midlatitude sporadic-E episodes viewed by L-band split-spectrum InSAR. *Earth Planets and Space*, *69*(175), 1–10. https://doi.org/10.1186/s40623-017-0764-6

Ghayournajarkar, N., & Fukushima, Y. (2020). Determination of the dipping direction of a blind reverse fault from InSAR: Case study on the 2017 Sefid Sang earthquake, northeastern Iran. *Earth Planets and Space*, *72*(64), 1–15. https://doi.org/10.1186/s40623-020-01190-6

Goldstein, R. M., & Werner, C. L. (1998). Radar interferogram filtering for geophysical applications. *Geophysical Research Letters*, *25*(21), 4035–4038. https://doi.org/10.1029/1998GL900033

Gomba, G., Parizzi, A., De Zan, F., Eineder, M., & Bamler, R. (2016). Toward operational compensation of ionospheric effects in SAR interferograms: The split-spectrum method. *IEEE Transactions on Geoscience and Remote Sensing*, *54*(3), 1446–1461. https://doi.org/10.1109/tgrs.2015.2481079

Hansen, P. C. (1992). Analysis of discrete Ill-Posed problems by means of the L-curve. *SIAM Review*, *34*(4), 561–580. https://doi.org/10.1137/1034115

Hansen, P. C., & O'Leary, D. P. (1993). The use of the L-curve in the regularization of discrete Ill-Posed problems. *SIAM Journal on Scientific Computing*, *14*(6), 1487–1503. https://doi.org/10.1137/0914086

Harris, R. A. (1998). Introduction to special section: Stress Triggers, stress Shadows, and implications for seismic hazard. *Journal of Geophysical Research*, *103*(B10), 24347–24358. https://doi.org/10.1029/98JB01576

Harris, R. A., & Simpson, R. W. (1992). Changes in static stress on southern California faults after the 1992 Landers earthquake. *Nature*, *360*(6401), 251–254. https://doi.org/10.1038/360251a0

He, P., Liu, C., Wen, Y., & Ding, K. (2024). Complex rupture features and triggering during the 2022 Chishang earthquake sequence in eastern Taiwan estimated by InSAR, GPS, strong motion, and teleseismic waveform evidence. *Seismological Research Letters*, *95*(4), 2092–2104. https://doi.org/10.1785/0220230358

Ho, C. S. (1986). A synthesis of the geologic evolution of Taiwan. *Tectonophysics*, *125*(1–3), 1–16. https://doi.org/10.1016/0040-1951(86)90004-1

Hsu, C.-C., & Wu, H.-Y. (2025). Using RSQSim to determine seismic sequence in eastern Taiwan fault system. *Seismological Research Letters*, *96*(1), 207–218. https://doi.org/10.1785/0220240144

Hsu, Y.-J., Rivera, L., Wu, Y.-M., Chang, C.-H., & Kanamori, H. (2010). Spatial heterogeneity of tectonic stress and friction in the crust: New evidence from earthquake focal mechanisms in Taiwan. *Geophysical Journal International*, *182*(1), 329–342. https://doi.org/10.1111/j.1365-246X.2010.04609.x

Hsu, Y.-J., Yu, S.-B., & Chen, H.-Y. (2009). Coseismic and postseismic deformation associated with the 2003 Chengkung, Taiwan, earthquake. *Geophysical Journal International*, *176*(2), 420–430. https://doi.org/10.1111/j.1365-246X.2008.04009.x

Hsu, Y.-J., Yu, S.-B., Simons, M., Kuo, L.-C., & Chen, H.-Y. (2009). Interseismic crustal deformation in the Taiwan plate boundary zone revealed by GPS observations, seismicity, and earthquake focal mechanisms. *Tectonophysics*, *479*(1–2), 4–18. https://doi.org/10.1016/j.tecto.2008.11.016

Hunter, J. D. (2007). Matplotlib: A 2D graphics environment. *Computing in Science & Engineering*, *9*(3), 90–95. https://doi.org/10.1109/mcse.2007.55

Institute of Earth Sciences, Academia Sinica, Taiwan. (1996). Broadband array in Taiwan for seismology [Dataset]. *International Federation of Digital Seismograph Networks*. https://doi.org/10.7914/SN/TW

Ishimaru, Y., Takada, Y., Ching, K.-E., & Chang, W.-L. (2025). Geodetic data and fault model of the 2022 Yuli earthquake in eastern Taiwan [Dataset]. *Zenodo*. https://doi.org/10.5281/zenodo.15287084

Jian, P.-R., Tseng, T.-L., Liang, W.-T., & Huang, P.-H. (2018). A new automatic full-waveform regional moment Tensor inversion algorithm and its applications in the Taiwan area. *Bulletin of the Seismological Society of America*, *108*(2), 573–587. https://doi.org/10.1785/0120170231

Jónsson, S., Zebker, H., Segall, P., & Amelung, F. (2002). Fault slip distribution of the 1999 M_w 7.1 Hector mine, California, earthquake, estimated from satellite radar and GPS measurements. *Bulletin of the Seismological Society of America*, *92*(4), 1377–1389. https://doi.org/10.1785/0120000922

Kanamori, H. (1977). The energy release in great earthquakes. *Journal of Geophysical Research*, *82*(20), 2981–2987. https://doi.org/10.1029/JB082i020p02981

King, G. C. P., Stein, R. S., & Lin, J. (1994). Static stress changes and the triggering of earthquakes. *Bulletin of the Seismological Society of America*, *84*(3), 935–953. https://doi.org/10.1785/BSSA0840030935

Lee, S.-J., Huang, H.-H., Shyu, J. B. H., Yeh, T.-Y., & Lin, T.-C. (2014). Numerical earthquake model of the 31 October 2013 Ruisui, Taiwan, earthquake: Source rupture process and seismic wave propagation. *Journal of Asian Earth Sciences*, *96*, 374–385. https://doi.org/10.1016/j.jseaes.2014.09.020

Lee, S.-J., Liu, T.-Y., & Lin, T.-C. (2023). The role of the west-dipping collision boundary fault in the Taiwan 2022 Chihshang earthquake sequence. *Scientific Reports*, *13*(1), 3552. https://doi.org/10.1038/s41598-023-30361-0

Lee, Y.-H., Chen, G.-T., Rau, R.-J., & Ching, K.-E. (2008). Coseismic displacement and tectonic implication of 1951 Longitudinal Valley earthquake sequence, eastern Taiwan. *Journal of Geophysical Research*, *113*(B4), B04305. https://doi.org/10.1029/2007JB005180

Lin, C.-R., Liao, Y.-C., Wang, C.-C., Kuo, B.-Y., Chen, H.-H., Jang, J.-P., et al. (2024). Development and evaluations of the Broadband Ocean Bottom Seismometer (Yardbird-BB OBS) in Taiwan. *Terrestrial, Atmospheric and Oceanic Sciences*, *35*(4), 1–12. https://doi.org/10.1007/s44195-024-00062-w

Lin, H.-F., Gualandi, A., Hsu, Y.-F., Hsu, Y.-J., Huang, H.-H., Lee, H.-M., & Canitano, A. (2023). Interplay between seismic and aseismic deformation on the central Range Fault during the 2013 M_w 6.3 Ruisui earthquake (Taiwan). *Journal of Geophysical Research: Solid Earth*, *128*(9), e2023JB026861. https://doi.org/10.1029/2023JB026861

Lin, H.-F., Hsu, Y.-F., & Canitano, A. (2023). Source modeling of the 2009 Fengpin–Hualien earthquake sequence, Taiwan, inferred from static strain measurements. *Pure and Applied Geophysics*, *180*(2), 715–733. https://doi.org/10.1007/s00024-022-03068-y

Lohman, R. B., & Simons, M. (2005). Some thoughts on the use of InSAR data to constrain models of surface deformation: Noise structure and data downsampling. *Geochemistry, Geophysics, Geosystems*, *6*(1), Q01007. https://doi.org/10.1029/2004GC000841

Menke, W. (2018). *Geophysical data analysis: Discrete inverse theory* (4th ed.), Academic Press. https://doi.org/10.1016/C2016-0-05203-8

Meyer, F., Bamler, R., Jakowski, N., & Fritz, T. (2006). The potential of low-frequency SAR systems for mapping ionospheric TEC distributions. *IEEE Geoscience and Remote Sensing Letters*, *3*(4), 560–564. https://doi.org/10.1109/LGRS.2006.882148

Mozziconacci, L., Delouis, B., Huang, B.-S., Lee, J.-C., & Béthoux, N. (2013). Determining Fault geometry from the distribution of coseismic fault slip related to the 2006 Taitung earthquake, eastern Taiwan. *Bulletin of the Seismological Society of America*, *103*(1), 394–411. https://doi.org/10.1785/0120110232

Okada, Y. (1985). Surface deformation due to shear and tensile faults in a half-space. *Bulletin of the Seismological Society of America*, *75*(4), 1135–1154. https://doi.org/10.1785/BSSA0750041135

Okada, Y. (1992). Internal deformation due to shear and tensile faults in a half-space. *Bulletin of the Seismological Society of America*, *82*(2), 1018–1040. https://doi.org/10.1785/BSSA0820021018

Peng, W., Radiguet, M., Pathier, E., & Chen, K. H. (2023). Fault coupling on a creeping thrust Fault: Joint inversion using geodetic data and repeating earthquakes. *Journal of Geophysical Research: Solid Earth*, *128*(9), e2023JB026843. https://doi.org/10.1029/2023JB026843

Pritchard, M. E., Simons, M., Rosen, P. A., Hensley, S., & Webb, F. H. (2002). Co-seismic slip from the 1995 July 30 M_w = 8.1 Antofagasta, Chile, earthquake as constrained by InSAR and GPS observations. *Geophysical Journal International*, *150*(2), 362–376. https://doi.org/10.1046/j.1365-246X.2002.01661.x

Rau, R.-J., & Wu, F. T. (1995). Tomographic imaging of lithospheric structures under Taiwan. *Earth and Planetary Science Letters*, *133*(3–4), 517–532. https://doi.org/10.1016/0012-821X(95)00076-O

Reasenberg, P. A., & Simpson, R. W. (1992). Response of regional seismicity to the static stress change produced by the Loma Prieta earthquake. *Science*, *255*(5052), 1687–1690. https://doi.org/10.1126/science.255.5052.1687

Reid, H. F. (1910). *The mechanics of the earthquake, the California earthquake of April 18, 1906. Report of the state Earthquake investigation commission* (Vol. 2). Carnegie Institution of Washington.

Rosen, P. A., Hensley, S., & Chen, C. (2010). Measurement and mitigation of the ionosphere in L-band interferometric SAR data. In *2010 IEEE Radar Conference* (pp. 1459–1463). https://doi.org/10.1109/RADAR.2010.5494385

Savage, J. C. (1983). A dislocation model of strain accumulation and release at a subduction zone. *Journal of Geophysical Research*, *88*(B6), 4984–4996. https://doi.org/10.1029/JB088iB06p04984

Shyu, J. B. H., Sieh, K., Avouac, J.-P., Chen, W.-S., & Chen, Y.-G. (2006). Millennial slip rate of the Longitudinal Valley fault from river terraces: Implications for convergence across the active suture of eastern Taiwan. *Journal of Geophysical Research*, *111*(B8), B08403. https://doi.org/10.1029/2005JB003971

Shyu, J. B. H., Sieh, K., Chen, Y.-G., & Chung, L.-H. (2006). Geomorphic analysis of the Central Range fault, the second major active structure of the Longitudinal Valley suture, eastern Taiwan. *Geological Society of America Bulletin*, *118*(11–12), 1447–1462. https://doi.org/10.1130/B25905.1

Shyu, J. B. H., Yin, Y.-H., Chen, C.-H., Chuang, Y.-R., & Liu, S.-C. (2020). Updates to the on-land seismogenic structure source database by the Taiwan Earthquake Model (TEM) project for seismic hazard analysis of Taiwan. *Terrestrial, Atmospheric and Oceanic Sciences*, *31*(4), 469–478. https://doi.org/10.3319/TAO.2020.06.08.01

Stein, R. S. (1999). The role of stress transfer in earthquake occurrence. *Nature*, *402*(6762), 605–609. https://doi.org/10.1038/45144

Stein, R. S., King, G. C. P., & Lin, J. (1992). Change in failure stress on the southern san Andreas fault system caused by the 1992 magnitude = 7.4 Landers earthquake. *Science*, *258*(5086), 1328–1332. https://doi.org/10.1126/science.258.5086.1328

Styron, R., & Pagani, M. (2020). The GEM global active faults database. *Earthquake Spectra*, *36*(1_suppl), 160–180. https://doi.org/10.1177/8755293020944182

Takada, Y., Fukahata, Y., Hashima, A., Terakawa, T., Fukui, K., Yanagisawa, T., et al. (2007). Development of three-dimensional basement structure in Taiwan deduced from past plate motion: Consistency with the present seismicity. *Tectonics*, *26*(3), TC3004. https://doi.org/10.1029/2006TC001957

Tang, C.-H., Lin, Y. N., Tung, H., Wang, Y., Lee, S.-J., Hsu, Y.-J., et al. (2023). Nearby fault interaction within the double-vergence suture in eastern Taiwan during the 2022 Chihshang earthquake sequence. *Communications Earth & Environment*, *4*(1), 333. https://doi.org/10.1038/s43247-023-00994-0

Tang, X., Guo, R., Li, L., Xu, Y., Xu, J., Zheng, Y., & Sun, H. (2025). Earthquake interactions in eastern Taiwan: Insight from the 2024 M_w 7.3 Hualien earthquake. *Seismological Research Letters*, *96*(1), 9–18. https://doi.org/10.1785/0220240230

Tarayre, H., & Massonnet, D. (1996). Atmospheric Propagation heterogeneities revealed by ERS-1 interferometry. *Geophysical Research Letters*, *23*(9), 989–992. https://doi.org/10.1029/96GL00622

Thomas, M. Y., Avouac, J.-P., Champenois, J., Lee, J.-C., & Kuo, L.-C. (2014). Spatiotemporal evolution of seismic and aseismic slip on the Longitudinal Valley Fault, Taiwan. *Journal of Geophysical Research: Solid Earth*, *119*(6), 5114–5139. https://doi.org/10.1002/2013JB010603

Toda, S., & Stein, R. S. (2020). Long- and short-term stress interaction of the 2019 ridgecrest sequence and coulomb-based earthquake forecasts. *Bulletin of the Seismological Society of America*, *110*(4), 1765–1780. https://doi.org/10.1785/0120200169

Toda, S., Stein, R. S., Sevilgen, V., & Lin, J. (2011). Coulomb 3.3 Graphic-rich deformation and stress-change software for earthquake. *Tectonic, and Volcano Research and Teaching—User Guide. U.S. Geological Survey Open-File Report 2011*, *1060*, 63.

Tozer, B., Sandwell, D. T., Smith, W. H. F., Olson, C., Beale, J. R., & Wessel, P. (2019). Global bathymetry and topography at 15 arc Sec: SRTM15+. *Earth and Space Science*, *6*(10), 1847–1864. https://doi.org/10.1029/2019EA000658

Tung, H., Chen, H.-Y., Hsu, Y.-J., Tang, C.-H., Lee, J.-C., Wang, Y., & Lee, H. K. (2025). Geodetic constraints on the September 2022 Guanshan and Chihshang earthquakes, eastern Taiwan. *Tectonophysics*, *895*, 230600. https://doi.org/10.1016/j.tecto.2024.230600

Uieda, L., Tian, D., Leong, W. J., Toney, L., Schlitzer, W., Grund, M., et al. (2021). PyGMT: A Python interface for the generic Mapping tools [Software]. *Zenodo*. https://doi.org/10.5281/zenodo.4522136

Wegmüller, U., & Werner, C. (1997). Gamma SAR processor and interferometry software. *Proceedings of Third ERS Symposium on Space at the service of our Environment (ESA SP-414)*, *3*, 1687–1692.

Wegmüller, U., Werner, C., Frey, O., Magnard, C., & Strozzi, T. (2018). Reformulating the split-spectrum method to facilitate the estimation and compensation of the ionospheric phase in SAR Interferograms. *Procedia Computer Science*, *138*, 318–325. https://doi.org/10.1016/j.procs.2018.10.045

Wegmüller, U., Werner, C., Strozzi, T., & Wiesmann, A. (2006). Ionospheric electron concentration effects on SAR and INSAR. In *2006 IEEE International Symposium on Geoscience and remote sensing* (pp. 3731–3734). https://doi.org/10.1109/IGARSS.2006.956

Wessel, P., Luis, J. F., Uieda, L. A., Scharroo, R., Wobbe, F., Smith, W. H. F., & Tian, D. (2019). The generic mapping tools version 6. *Geochemistry, Geophysics, Geosystems*, *20*(11), 5556–5564. https://doi.org/10.1029/2019GC008515

Wicks, C. W., Jr., Dzurisin, D., Ingebritsen, S., Thatcher, W., Lu, Z., & Iverson, J. (2002). Magmatic activity beneath the quiescent Three Sisters volcanic center, central Oregon Cascade Range, USA. *Geophysical Research Letters*, *29*(7), 26. https://doi.org/10.1029/2001GL014205

Wu, Y.-M., Chen, Y.-G., Chang, C.-H., Chung, L.-H., Teng, T.-L., Wu, F. T., & Wu, C.-F. (2006). Seismogenic structure in a tectonic suture zone: With new constraints from 2006 Mw6.1 Taitung earthquake. *Geophysical Research Letters*, *33*(22), L22305. https://doi.org/10.1029/2006GL027572

Wu, Y. M., Chen, Y. G., Shin, T. C., Kuochen, H., Hou, C. S., Hu, J. C., et al. (2006). Coseismic versus interseismic ground deformations, fault rupture inversion and segmentation revealed by 2003 *Mw* 6.8 Chengkung earthquake in eastern Taiwan. *Geophysical Research Letters*, *33*(2), L02312. https://doi.org/10.1029/2005GL024711

Wu, Y.-M., Zhao, L., Chang, C.-H., & Hsu, Y.-J. (2008). Focal-mechanism determination in Taiwan by Genetic algorithm. *Bulletin of the Seismological Society of America*, *98*(2), 651–661. https://doi.org/10.1785/0120070115

Yagi, Y., Okuwaki, R., Enescu, B., & Lu, J. (2023). Irregular rupture process of the 2022 Taitung, Taiwan, earthquake sequence. *Scientific Reports*, *13*(1), 1107. https://doi.org/10.1038/s41598-023-27384-y

Yang, Y.-H., Li, L., Hu, J.-C., Tung, H., Xu, Q., Li, X., et al. (2024). Double-vergent plate boundary faults and triggered coseismic rupture of the 2022 Chihshang doublet earthquake occurred in eastern Taiwan. *Seismological Research Letters*, *95*(4), 2081–2091. https://doi.org/10.1785/0220230026

Yu, C., Li, Z., Penna, N. T., & Crippa, P. (2018). Generic atmospheric correction model for interferometric synthetic aperture Radar observations. *Journal of Geophysical Research: Solid Earth*, *123*(10), 9202–9222. https://doi.org/10.1029/2017JB015305

Zumberge, J. F., Heflin, M. B., Jefferson, D. C., Watkins, M. M., & Webb, F. H. (1997). Precise point positioning for the efficient and robust analysis of GPS data from large networks. *Journal of Geophysical Research*, *102*(B3), 5005–5017. https://doi.org/10.1029/96JB03860